OPEN ACCESS

University of BRISTOL

Peer reviewed version

Link to published version (if available):
10.1016/j.epsl.2017.01.029

Link to publication record in Explore Bristol Research
PDF-document

University of Bristol - Explore Bristol Research
General rights

1 **Precession driven changes in terrestrial organic matter input**

2 **to the Eastern Mediterranean leading up to the Messinian**

3 **Salinity Crisis**

4 Jan Peter Mayser [a,b,*], Rachel Flecker [b,c], Alice Marzocchi [b,c,1] , Tanja J. Kouwenhoven [d],

5 Dan J. Lunt [b,c], Rich D. Pancost [a,b]

6

7 [a] Organic Geochemistry Unit, School of Chemistry, University of Bristol, Cantock's Close,

8 Bristol BS8 1TS, UK

9 [b] BRIDGE, School of Geographical Sciences, University of Bristol, University Road, Bristol

10 BS8 1SS, UK

11 [c] Cabot Institute, University of Bristol, Bristol BS8 1UJ, UK

12 [d] Department of Geosciences, Utrecht University, Heidelberglaan 2, 3584 CS Utrecht,

13 The Netherlands

Abstract

14

15 Eastern Mediterranean sediments over the past 12 Myr commonly show strongly

16 developed precessional cyclicity, thought to be a biogeochemical response to insolation-

17 driven freshwater input from run-off. The Mediterranean's dominant freshwater source today

18 and in the past, is the Nile, which is fed by North African monsoon rain; other, smaller, circum-

19 Mediterranean rivers also contribute to Mediterranean hydrology. Crucially, run-off through

20 all of these systems appears to vary with precession, but there is no direct evidence linking

[1] current address: Department of the Geophysical Sciences, The University of Chicago, USA

21   individual water sources to the biogeochemical response recorded in Mediterranean

22   sediments. Consequently, it is not clear whether the North African monsoon is entirely

23   responsible for the Mediterranean's sedimentary cyclicity, or whether other, precessional

24   signals, such as Atlantic storm precipitation, drive it.

25   Organic matter in sediments derives from both marine and terrestrial sources and

26   biomarker analysis can be used to discriminate between the two, thereby providing insight

27   into sedimentary and ecological processes. We analysed a wide range of lipids from the Late

28   Miocene (6.6-5.9 Ma) Pissouri section, southern Cyprus, and reconstructed the vegetation

29   supplied to this region by measuring the carbon isotopes of the terrestrial component to

30   identify its geographic source. BIT (Branched-Isoprenoidal-Tetraether) indices reflect changes

31   in the relative abundance of marine vs terrestrial (soil) organic matter inputs, and with the

32   exception of records from the last deglaciation, this work is the first application of the BIT

33   approach to the reconstruction of orbital impacts on sedimentological processes. BIT indices

34   show that the organic matter supplied to Cyprus changed over the course of each precession

35   cycle and was dominantly terrestrial during insolation maxima when North African run-off was

36   enhanced. The δ^{13}C values from these intervals are compatible with tropical North African

37   vegetation. However, the δ^{13}C record indicates that during insolation minima, organic material

38   supplied to southern Cyprus derives from a more arid source region. This is likely to have been

39   aeolian-transported organic matter from the Anatolian Plateau demonstrating that even in

40   Mediterranean sedimentary systems influenced by Nile run-off, there is more than one

41   independent precessional organic matter contribution to the sedimentary cyclicity. Pissouri's

42   organic geochemistry also illustrates a long-term trend towards more saline Mediterranean

43   conditions during the 600 kyr leading up to the Messinian Salinity Crisis.

Highlights

44

- BIT index shows major precessional changes in run-off to the Mediterranean.

45

- $\delta^{13}C$ record of higher plant waxes also varies with precession

46

- Cyprus receives organic matter input from both North Africa and Turkey

47

- New SST record leading up to the Messinian Salinity Crisis

48

- Long-term biomarker trends indicate the looming Messinian Salinity Crisis

49

Keywords:

50

Mediterranean; BIT index; carbon isotopes; Messinian Salinity Crisis; terrestrial higher

51

plant waxes; TEX_{86}

52

1   Introduction

53

Mediterranean sedimentary successions over the last 12 million years (Ma) are

54

commonly dominated by strong cyclicity (Kidd et al., 1978; Rohling et al., 2015). These regular

55

lithological alternations, comprising some combination of marls, limestones, diatomites and

56

organic-rich sapropelic layers, are demonstrably precessional (Hilgen et al., 1997; Sierro et al.,

57

2001) and are thought to be the Mediterranean's biogeochemical response to orbitally-driven

58

variations in freshwater input (Rossignol-Strick, 1985). The largest source of this freshwater

59

variation is derived from the North African monsoon (Rohling et al., 2015 and references

60

therein). Precessional changes shift the position of the Intertropical Convergence Zone (ITCZ)

61

northward during times of insolation maxima (July 65N; Laskar et al., 2004) and increase the

62

intensity of the monsoon in the catchment of northward draining rivers that flow into the

63

Mediterranean (Marzocchi et al., 2015). These insolation-driven changes also affect the

64

vegetation across North Africa (Larrasoaña et al., 2013), although model simulations fail to

65

66 capture the full greening of the Sahara indicated by terrestrial data (Larrasoaña et al., 2013

67 and references therein). Precessional changes in the location and intensity of North Atlantic

68 storm tracks also impact Mediterranean precipitation patterns, principally in the west and

69 along the north Mediterranean margin (Kutzbach et al., 2014; Toucanne et al., 2015).

70   In the Late Miocene Mediterranean salinity rose significantly and thick, basin-wide

71 evaporites were deposited during the Messinian Salinity Crisis (MSC, 5.971-5.33 Ma; Manzi et

72 al., 2013 and references therein). While deep basinal evaporites have yet to be recovered,

73 those preserved on the Mediterranean margins also show strong cyclicity which is thought to

74 reflect an on-going precessional signal (Flecker et al., 2015), despite extreme environmental

75 conditions. Although the transition to evaporite precipitation in the Mediterranean is

76 synchronous and abrupt at 5.97 Ma (Manzi et al., 2013), geochemical evidence (Flecker et al.,

77 2015 and references therein) as well as water column oxygenation and faunal data

78 (Kouwenhoven et al., 2003; Sierro et al., 2001) indicate that the first environmental precursors

79 of the MSC occurred several million years earlier.

80   The evidence of precessional-pacing of Mediterranean sedimentation is clear. However,

81 the specific processes that generated the recorded biogeochemical response remain

82 controversial. Debates over the role of freshwater driven productivity versus water column

83 stratification in the generation of organic-rich sapropelic layers (Kidd et al., 1978) endure,

84 while the question of whether deep-sea anoxia, promoted by enhanced export productivity,

85 a freshwater cap, or a combination of both, can transfer the precessional run-off signal from

86 the Eastern to Western Basins as advocated by Rohling et al. (2015), remains untested. One

87 alternative possibility is that the North Atlantic storm-track generates the precessional

88 biogeochemical response in the Western Mediterranean independent of, but in phase with

89 precessional run-off to the Eastern Mediterranean (Toucanne at al. 2015). However, it is not

90   clear whether the storm track precipitation is volumetrically sufficient to generate the

91   biogeochemical response observed.

92   All of these controversies relate, in part, to the difficulty in identifying the fresh water

93   sources responsible for driving the biogeochemical sedimentary product observed in the

94   Mediterranean Basin. This study uses biomarkers preserved within the sedimentary record as

95   tracers of the freshwater from which they were derived in order to explore and provide new

96   insight into the underlying dynamics of the Mediterranean's sedimentary cyclicity.

97   Lipid biomarkers have been used to explore changes in the hydrological cycle in a variety

98   of ways. Leaf wax δ^{13}C values differ between C$_3$-and C$_4$-plants where C$_3$-plants have lower δ^{13}C

99   values than C$_4$-plants (O'Leary, 1981) as a result of their different morphology and carbon

100   assimilation biochemistry (Edwards et al., 2010 and references therein). Because the

101   distribution of C$_3$- and C$_4$-plants is governed by a combination of environmental factors,

102   including temperature and aridity (Yang et al., 2014), leaf wax δ^{13}C values provide insight into

103   both past vegetation and climatic conditions. Biomarkers can also provide insight into changes

104   in marine versus terrestrial organic matter (OM) fluxes (Hopmans et al., 2004), from which

105   changes in the OM source can be inferred. Other lipid biomarkers, including isoprenoidal and

106   branched glycerol dialkyl glycerol tetraether (GDGT) lipids can be used to determine sea-

107   surface temperatures (TEX$_{86,}$ [TetraEther indeX]; Schouten et al., 2013 and references therein)

108   and land surface temperatures (MBT' [Methylation of Branched Tetraether]/CBT [Cyclisation

109   of Branched Tetraethers]; Weijers et al., 2007; Peterse et al., 2012), providing additional

110   insights into environmental changes. This approach constrains the relative control of

111   temperature versus aridity on C$_3$/C$_4$ plant abundances.

112   We have applied these approaches to the Late Miocene Pissouri section on Cyprus

113   (5.98-6.51 Ma), which lies to the north of the Nile delta (Fig. 1). Today, the majority of the

114   monsoon-derived North African run-off reaches the Mediterranean via the Nile which is its

115   largest fluvial system. We extracted and characterised biomarkers from the strongly cyclic

116   Pissouri succession and have used them to reconstruct the influence of Nile water and the

117   precipitation in its catchment. In particular, we use the proportions branched-GDGTs

118   (brGDGTs) to crenarchaeol (BIT index), distributions of n-alkyl lipids, and the δ^{13}C values of

119   high molecular weight n-alkanes of terrestrial plant origin, to establish the nature of organic

120   matter supplied to this central eastern Mediterranean region. The ~600 kyr interval preceding

121   the MSC was targeted in order to evaluate the climatic changes that occur during the leading

122   up to the MSC.

123   **2   Methods**

124   ***2.1   Site description and sampling strategy***

125   The Pissouri basin on southern Cyprus (Fig. 1) is filled with Neogene sediments

126   extending back to the Middle Miocene (Krijgsman et al., 2002). The Messinian succession of

127   the basin comprises regular alternations of limestones and marls (Fig. 2; Krijgsman et al.,

128   2002) where carbonate content (Krijgsman et al., 2002) has been used to distinguish them

129   (e.g. limestone >75%; marl <75%; Sugden and McKerrow, 1962). The cyclicity of the succession

130   has been used to astronomically tune the Pissouri section to orbital solutions (Laskar et al.,

131   2004) using both bio- and magnetostratigraphic tie-points (Fig. 2; Krijgsman et al., 2002). At

132   Pissouri, three biostratigraphic events occur in the 30 m of limestone-marl alternations that

133   directly underlie the gypsum and are studied here (Fig. 2). These biostratigraphic tie points

134   consistently link marl deposition to the area of the orbital curve that includes the insolation

135   maxima (Fig. 2). In addition, three magnetostratigraphic boundaries also occur in this part of

136   the section (Fig. 2) and these are consistent with the tuning based on biostratigraphic tie-

137   points and confirm the lithological phase relationship with the orbital curve (Krijgsman et al.,

138   2002). The marls have been correlated with sapropelic horizons (Krijgsman et al., 2002) that

139   are observed in other Mediterranean successions (e.g. Sorbas; Sierro et al., 2001). In line with

140   standard practice for astronomically tuned Mediterranean successions and consistent with

141   the biostratigraphic and magnetostratigraphic tie points, the middle of each marl (or sapropel)

142   layer is linked to the extremes of the 65N summer insolation curve (Sierro et al., 2001; Fig 2.).

143   Forty-eight samples were collected in 1998 from the Pissouri section road cut

144   (Kouwenhoven et al., 2006; Krijgsman et al., 2002) before it was sprayed with concrete. Where

145   possible, one sample for every limestone and one for every marl was analysed throughout the

146   section, starting at ~32 m below the gypsum and representing the 600 kyr preceding the MSC

147   (6.519- 5.983; Ma Krijgsman et al., 2002). While this approach does not necessarily show the

148   full range of values in relation to precession, it does allow us to compare data generated

149   during two distinct phases of multiple orbital cycles. The slump layer (7-10 m Fig. 2) towards

150   the top of the section was not sampled because its age and orbital phasing is uncertain.

151   ### 2.2   *Extraction and Separation*

152   The sediments (~40g) were homogenised and extracted via Soxhlet apparatus for 24

153   hours using dichloromethane (DCM): methanol (MeOH) (2:1 vol/vol). An aliquot of the total

154   lipid extract (TLE) was separated into two fractions using alumina flash column

155   chromatography: an apolar fraction eluted with 4 ml hexane (Hex)/DCM (9:1 v/v) and a polar

156   fraction eluted with 3 ml DCM:MeOH (1:2 vol/vol). An internal standard (IS) was added to the

157   apolar (androstane 5µl of 200 ng/µl) and polar (hexadecan-2-ol, 5 µl, 207.5 mg/µl solution)

158   fractions. The polar fraction was derivatised for 1 hour at 70°C using 50µl of BSTFA+TMCS 99:1

159   (N,O-bis(trimethylsilyl) trifluoroacetamide and trimethylchlorosilane).

2.3   GC-MS

Both fractions were analysed using a Thermo Scientific ISQ Single Quadrupole gas

chromatography-mass spectrometer (GC-MS). The GC was equipped with a 50 m x 0.32 mm

i.d. fused silica capillary column with an Rtx-1 stationary phase (100% dimethylpolysiloxane,

0.17 μm film thickness; Restek) and programmed from 70 °C (held for 1 minute) to 130 °C at

20 °C/minute, then to 300 °C (held for 24 minutes) at 4 °C/minute. The MS continuously

scanned between mass to charge ratios *m/z* 50 and 650 Daltons. The *n*-alkanes, *n*-alkanols

and *n*-alkanoic acids were identified by their spectra and quantified in the total ion current.

2.3.1   GC-C-IRMS

The *n*-alkane $\delta^{13}C$ values were determined using an Isoprime 100 GC-combustion-

isotope ratio MS (GC-C-IRMS). Apolar fractions were analysed in duplicate, injected via a

splitless injector onto a 50 m x 0.32 i.d. fused silica capillary column with an HP 1 stationary

phase (100% dimethylpolysiloxane, 0.17 film thickness, Agilent). The temperature programme

was the same as for GC-MS analysis. The combustion reactor was maintained at a temperature

of 850 °C. Standard notation relative to the Vienna Pee Dee Belemnite (VPDB) was achieved

by comparison against a calibrated reference CO_2 gas. Two thirds of samples had sufficient *n*-

alkane abundances for $\delta^{13}C$ determination.

2.3.2   HPLC-APCI-MS

The second aliquot of the TLE was dissolved in A (A=hexane:iso-propanol (IPA) (99:1

v/v)) and passed through a 0.45 μm PTFE filter. High performance liquid chromatography-

atmospheric pressure chemical ionisation-MS (HPLC-APCI-MS) was performed using a

ThermoFisher Scientific Accela Quantum Access triple quadrupole MS to analyse the iGDGTs

and brGDGTs. Separation was achieved with an Alltech Prevail Cyao column (150 mm; 2.1 mm;

183   3μm i.d.) with a flow rate of 0.2 ml/minute. The initial solvent mix A was eluted isocratically

184   for 5 minute, followed by a change in solvent polarity via a gradient to 1.8% IPA over 45

185   minutes (Hopmans et al., 2000). After separation, ionisation was performed at atmospheric

186   pressure, and select m/z: 1302, 1300, 1298, 1296, 1294, 1292, 1050, 1048, 1046, 1036, 1034,

187   1032, 1022, 1020, 1018, 744, 659 (Fig.3; Schouten et al., 2013) were scanned to increase

188   sensitivity and reproducibility. GDGT ratios were calculated from the respective M^+-ions

189   chromatograms, and abundances were determined by comparing with a known C_{46}-GDGT

190   standard (Huguet et al., 2006). The relative response of the standard and the GDGTs was not

191   determined, such that reported concentrations are strictly semi-quantitative.

192   **2.3.3   Proxies**

193   Long-chain n-alkanes are synthesised by terrestrial vascular plants (Eglinton and

194   Hamilton, 1967). The carbon preference index (CPI) is the ratio of odd-to-even chain lengths

195   of the n-alkanes and is calculated as follows:

196   $$\text{CPI} = 0.5 * \left(\frac{C_{23} + C_{25} + C_{27} + C_{29} + C_{31} + C_{33}}{C_{24} + C_{26} + C_{28} + C_{30} + C_{32} + C_{34}} + \frac{C_{23} + C_{25} + C_{27} + C_{29} + C_{31} + C_{33}}{C_{22} + C_{24} + C_{26} + C_{28} + C_{30} + C_{32}} \right)$$

Equation 1: CPI (Bray and Evans, 1961)

197   The components of Equation 1 refer to the relative concentrations of C_{22} to C_{32} n-

198   alkanes. During biosynthesis, higher plants produce high-molecular-weight (HMW) odd-

199   numbered n-alkanes (Eglinton and Hamilton, 1967), but subsequent diagenesis (and

200   catagenesis) causes homogenisation of the distribution (Bray and Evans, 1961). Consequently,

201   lower CPI values can indicate increased degradation of these terrestrial inputs or a change in

202   their source, whereas values >2 indicate good preservation.

203   The terrestrial aquatic ratio ($TAR_{n\text{-alkanes}}$) for the n-alkanes is calculated as:

204   $$\text{TAR}_{n-\text{alkanes}} = \frac{C_{27} + C_{29} + C_{31}}{C_{15} + C_{17} + C_{19}}$$

Equation 2: TAR (Bourbonniere and Meyers, 1996)

205   This can be used to evaluate sources of OM, because HMW *n*-alkanes are generally

206   produced by terrestrial vascular plants (Eglinton and Hamilton, 1967), and low-molecular-

207   weight (LMW) *n*-alkanes generally derive from aquatic organisms (Meyers and Arnaboldi,

208   2008 and references therein). Similar ratios can be calculated using *n*-alkanoic acids

209   (Bourbonniere and Meyers, 1996):

210    $$\mathrm{TAR}_{n-\mathrm{alkanoic\ acids}} = \frac{C_{26} + C_{28}}{C_{14} + C_{16} + C_{18}}$$

Equation 3: TAR$_{n\text{-alkanoic acids}}$ (Bourbonniere and Meyers, 1996)

211   The BIT index is a ratio of the three major brGDGTs to crenarchaeol:

212    $$\mathrm{BIT} = \frac{(\mathrm{GDGT} - \mathrm{Ia}) + (\mathrm{GDGT} - \mathrm{IIa}) + (\mathrm{GDGT} - \mathrm{IIIa})}{(\mathrm{Crenarcheaol}) + (\mathrm{GDGT} - \mathrm{Ia}) + (\mathrm{GDGT} - \mathrm{IIa}) + (\mathrm{GDGT} - \mathrm{IIIa})}$$

Equation 4: BIT Index (Hopmans et al., 2004)

213   Crenarchaeol is derived from Thaumarchaeota (Sinninghe Damsté et al., 2002), which

214   represents ~20% of the picoplankton in the ocean, although it also occurs in subordinate

215   abundances in soils (Weijers et al., 2007). BrGDGTs occur in high abundances in terrestrial

216   settings, including soils and peats (Hopmans et al., 2004; Peterse et al., 2012). Therefore, BIT

217   indices close to 1 represent OM originating from a predominantly terrigenous source, whereas

218   low indices represent a Thaumarchaeotal source of GDGTs and by extension a strong aquatic

219   source of OM (Schouten et al., 2013).

220   For the sea-surface temperature reconstructions, the TEX$_{86}$ proxy is defined as:

221    $$\mathrm{TEX}_{86} = \frac{\mathrm{GDGT} - 2 + \mathrm{GDGT} - 3 + \mathrm{Crenarcheaol}'}{\mathrm{GDGT} - 1 + \mathrm{GDGT} - 2 + \mathrm{GDGT} - 3 + \mathrm{Crenarcheaol}'}$$

Equation 5: TEX$_{86}$-proxy (Schouten et al., 2013)

222   Various calibrations have been proposed to transform TEX$_{86}$ values to sea-surface

223   temperature (SST), including both the original linear (Schouten et al., 2013) and subsequent

224   logarithmic (Kim et al., 2010) relationships. Here, we use the BAYSPAR-calibration, which

225   enables an increased accuracy and precision of reconstructions, due to the inclusion of a

226   spatial element in the calibration (Tierney and Tingley, 2015), as well as more robust Bayesian-

227   derived error estimates. It applies the modern core-top data and searches for modern

228   analogue locations based on the TEX_{86} index (Tierney and Tingley, 2015). Biomarker data (i.e.

229   hopane distributions) indicate that Pissouri OM is thermally immature, justifying the

230   application of this core-top approach to these uplifted marine sediments.

231   For the land-based temperature reconstructions the MBT'/CBT index is used:

232    $$CBT = \log \frac{GDGTIb + GDGTIIb}{GDGTIa + GDGTIIa}$$

233    $$MBT' = \frac{GDGTIa + GDGTIb + GDGTIc}{GDGTIa + GDGTIb + GDGTIc + GDGTIIa + GDGTIIb + GDGTIIc + GDGTIIIa}$$

Equation 6: MBT'/CBT proxy (Peterse et al., 2012)

234   In soils, the degree of cyclisation of branched GDGTs (reflected in the CBT index) is

235   correlated with pH, whereas the degree of methylation (MBT') is correlated with both pH and

236   Mean Annual Air Temperature (MAAT), resulting in the MBT(')/CBT soil temperature proxy

237   (Weijers et al., 2007, Peterse et al., 2012). This proxy is commonly applied to marginal marine

238   sediments to reconstruct the terrestrial climate of the catchment area (e.g. Peterse et al.,

239   2012). Since these analysis were completed, a new methodology has been proposed by De

240   Jonge et al. (2014) to include 6-methyl brGDGTs as well as the 5-methyl brGDGTs in the CBT

241   and MBT' proxies. GDGT abundances are low in these Pissouri samples, so there was

242   insufficient material to enable reanalysis and the application of this new method.

243   **3   Results**

244   All samples contained a variety of biomarkers, including both branched (brGDGT) and

245   isoprenoidal (iGDGT) GDGTs (Fig. 3) and a homologous series of *n*-alkanes and *n*-alkanoic

246   acids. Also present was an unusual nonacosan-10-ol which can be derived from conifers (Jetter

247   and Riederer, 1995).

248   ***3.1   GDGTs***

249   The Pissouri sediments contain a wide range of br- and iGDGTs (Fig. 3; data table;

250   Schouten et al., 2013). BIT indices are highly variable in the Pissouri sediments (Fig. 4c),

251   ranging from below 0.1 to 0.85, indicating more than one OM source. These variations are

252   strongly related to lithology, where the marls have significantly higher (Student's paired t-test

253   between BIT values of marls vs limestones $p<0.0001$) BIT indices (0.3 to 0.9) than the

254   limestones (0.1 to 0.6; Fig. 4c). There is a general decline in the limestone BIT indices from 0.6

255   to 0.05, up section (Fig. 4c). BIT indices from the marls have a more complex pattern, with

256   high BIT indices (0.67-0.90) in sediments older than 6.26 Ma and in those overlying the slump

257   (0.67-0.88) and lower indices in the intervening interval (0.17-0.65). Consequently, the

258   difference in marl-limestone BIT indices is most pronounced at the top and bottom of the

259   section, with a smaller marl-limestone contrast in BIT indices between 6.3 Ma and the slump

260   (Fig. 4c), mainly due to lower values in the marls.

261   The low BIT-contrast interval immediately below the slump is also characterised by

262   variable i- and brGDGTs abundances (Fig. 4d), with some values approximately two orders of

263   magnitude higher than in the rest of the section.

264   Br- and iGDGTs can also be used to determine terrestrial and sea-surface temperatures

265   (see Section 2.3.3). However, TEX$_{86}$ should not be applied to sediments with high BIT indices

266   (>0.4; Schouten et al., 2013 and references therein), and terrestrial temperatures should be

267   treated with caution in samples with low (<0.3, Weijers et al., 2007) BIT indices. In the Pissouri

268   section, 24 samples had BIT indices lower than 0.4, indicating the dominance of marine GDGTs

269   (Hopmans et al., 2004); in these, the TEX_{86}-derived SSTs range from 22°-30°C (data table) using

270   the BAYSPAR calibration (Tierney and Tingley, 2015). The 32 samples with BIT indices > 0.3,

271   yield MBT'/CBT-derived MAAT for the adjacent land ranging from 15° to 28° C (data table)

272   based on the calibration of (Peterse et al., 2012).

273   *3.2   N-alkyl biomarkers*

274   The overall distribution of the *n*-alkanoic acids in the Pissouri samples is bimodal, with

275   a peak at *n*-C_{16} and a second peak at *n*-C_{28}. In most cases the *n*-C_{28} *n*-alkanoic acid is most

276   abundant. The $TAR_{n\text{-alkanoic acid}}$ values vary from 0.7 to 2.2 (Fig. 5e). Commonly the limestones

277   have lower TARs than the marl layers (Fig. 5e), but this difference is less consistent than in the

278   BIT indices (Fig. 4c).

279   The *n*-alkane distribution is similar to the bimodal *n*-alkanoic acid distribution with one

280   short-chain peak (C_{19} although C_{15} and C_{17} homologues are also abundant) and another long-

281   chain maximum (C_{31}). The concentrations of the HMW *n*-alkanes range between 0.6 and 12

282   ng/g sediment (Fig. 5a), and is generally lower in the limestones. Between 6.35 and 6.15 Ma

283   the offset between the two lithologies is particularly clear, with higher *n*-alkane

284   concentrations occurring in the marls (Fig. 5a). The $TAR_{n\text{-alkanes}}$ ratio (data table) varies from

285   0.05 to 3.16 with an average of 0.36, but unlike the BIT indices, the $TAR_{n\text{-alkanes}}$ (Fig. 5b) show

286   no systematic relationship with lithology, potentially due to the complex range of biological

287   sources for the LMW components or a diverse range of higher plant inputs (i.e. aeolian vs

288   fluvial inputs) for the HMW components. At the top of the section, the $TAR_{n\text{-alkanes}}$ shift to

289   higher indices, i.e. higher concentrations of long chain *n*-alkanes indicating stronger terrestrial

290   inputs (Fig. 5b).

291   With one exception, all sediments have a CPI >1 (Fig. 5d; data table) with an average

292   value of 6 and a range from 2 to 8. This indicates a strong predominance of odd-over-even

293   HMW *n*-alkanes, compatible with a leaf wax source and good preservation (Bray and Evans,

294   1961). We have excluded the sample at 6.11 Ma (R.F.-7013f; data table) from further

295   discussion, because of its anomalously low CPI and position close to the slump interval.

296   Nonacosan-10-ol, which is derived from specific conifers (Jetter and Riederer, 1995), is

297   found throughout the section (Fig. 5c). Concentrations do not vary systematically with

298   lithology, but, with the exception of one highly concentrated sample at 6.2 Ma, the relatively

299   constant Nonacosan-10-ol concentration that characterises the lower part of the succession

300   up to 6.1 Ma is followed by a trend towards higher concentrations (6.08 - 5.98 Ma).

301   **3.3   Carbon isotopes of the long-chain *n*-alkanes**

302   In the Pissouri section, $\delta^{13}C$ values for the HMW C_{29}, C_{31} and C_{33} *n*-alkanes (Fig. 6) range

303   between -35‰ and -26‰. This range is more negative than the $\delta^{13}C$ values typically

304   associated with leaf waxes from C_4-plants (Kohn, 2016 and references therein), but is

305   consistent both with $\delta^{13}C$ values measured on C_3 plants or a mixture of C_4 and C_3 plants (Fig.

306   6). In the upper part of the section (younger than 6.22 Ma), $\delta^{13}C$ values for all three long-chain

307   *n*-alkanes are consistently lower by 2-3‰ in the limestones, than in the marls with which they

308   are interbedded (Fig. 6). In the lower part of the section low *n*-alkane abundances prevented

309    $\delta^{13}C$ analysis in 10 samples (~21% of dataset). However, where measured, *n*-alkanes in

310   limestones have lower $\delta^{13}C$ values than those in the adjacent marls.

4   Discussion

4.1   Temperature proxies

As discussed above, GDGTs are used to reconstruct both land and marine palaeo-temperatures. The high variability of marine versus terrestrial source inputs (Fig. 7a) at Pissouri allows both the marine and the terrestrial temperatures to be evaluated but only for specific horizons. Where BIT indices are <0.4 (Fig. 7b; Schouten et al., 2013 and references therein), TEX_{86}-derived SSTs are in good agreement with alkenone-derived SST records from Monte dei Corvi, Italy (Tzanova et al., 2015; Fig. 7a). The combined datasets indicate a cooling of the Eastern Mediterranean prior to the onset of the MSC (Fig. 7), consistent with a global Late Miocene cooling (Herbert et al, 2016). The average temperature of the Eastern Mediterranean today is 20-22°C, several degrees cooler than that indicated by the average SST for these Late Miocene samples (25.5°C; Fig. 7a) even when including the TEX_{86} uncertainty of 2-3° (Tierney and Tingley, 2015). The long-term temperature change is overprinted by shorter-term variability of 6°C (Fig. 7). The 12-13 kyr resolution of both our TEX_{86} and the alkenone (Tzanova et al., 2015) datasets means that we cannot be sure that this reflects the full range of precessional temperature variability.

The terrestrial MBT'/CBT-derived MAAT records appear to suggest an average temperature of 18°C with large temperature variations of up to 14°C (Fig. 7c); much larger than those seen in the SST reconstruction (Fig. 7a). However, the average is lower than that observed today (20°C) and the large variability is unexpected, even given the large standard error on MBT'/CBT-derived MAAT reconstructions of +/- 5°C (Peterse et al., 2012). There are several likely reasons for the pronounced variations.

 1. New analytical methods have been developed (De Jonge et al., 2014), and these could affect both determination of MBT indices and the application of appropriate calibrations.

335   We consider this factor to be minor given that much previous work based on the original

336   methods and calibrations still exhibited clear temporal trends.

337   2. The dataset includes samples with low BIT indices, which could be problematic (Weijers

338   et al., 2007); however, removing those data with BIT below 0.3 yields an average MAAT

339   of 18°C and a range of 15° to 28°C, still much larger than expected.

340   3. Recent work has repeatedly shown that MBT'/CBT indices yield relatively low MAATs in

341   arid settings (Peterse et al., 2012; Yang et al., 2014). Using a recently developed aridity

342   calibration, shifts the temperatures to higher values by ~ 2°C (Yang et al., 2014), and given

343   the fact that aridity is likely to have varied in the source region, this could be another

344   source of variability.

345   Overall, it appears that GDGT-based proxies confirm that the Eastern Mediterranean

346   was warmer during the Lateiocene than it is today, consistent with globally higher

347   temperatures (e.g. Tzanova et al., 2015) and model simulations using elevated pCO$_2$

348   (Marzocchi et al., 2015). Elevated MAATs are less clear, given the profound variability in

349   brGDGT indices, but we attribute this to complex changes in sources of brGDGTs and the

350   additional impact of highly variable hydrology (Yang et al., 2014).

351   ***4.2   Differences in limestone and marl OM inputs***

352   There is a statistically significant difference between the BIT indices of the limestones

353   and those of the marls (P>0.001; students t-test; Fig. 4c), probably as a result of varying OM

354   sources and preservation controls. The BIT index can be affected by OM degradation, with

355   preferential degradation of marine OM over terrestrial OM shifting BIT indices higher (Huguet

356   et al, 2009). Indeed, enhanced preservation beneath the slump is suggested by the higher

357   GDGT concentrations (Fig. 4d) and this may account for the abrupt shift to lower BIT indices

358   in the marls from this interval (Fig. 4c). In other intervals, however, the GDGT concentrations

359   exhibit much less variability and no systematic change with lithology suggesting that

360   differential OM degradation is not the primary driver of cyclic BIT variations. This is consistent

361   with previous work where Huguet et al. (2009) showed that extreme changes in redox

362   conditions, between oxic and anoxic sediments with the same OM input, can result in changes

363   in the BIT index preserved, but only by up to 0.4. The BIT variations we see here are >0.4 and

364   therefore cannot be entirely attributable to oxic degradation. In addition, the presence of

365   benthic foraminifera in both limestones and marls (Kouwenhoven et al., 2006) suggests that

366   oxygen fluctuations were never extreme enough to induce total anoxia. Elevated proportions

367   of the benthic foraminifera, *Bolivina spathulata* (70-90%), however, indicate that, as early as

368   7.167 Ma the sediments were also never fully oxic , and changes in redox conditions from less

369   to more severe dysoxia on a precessional time scale are apparent from repeated shifts in

370   benthic foraminifer assemblages after 6.4 Ma (Kouwenhoven et al., 2006 and references

371   therein). Consequently, the redox-driven preservational impact on BIT indices is likely to be

372   small.

373   Instead, we suggest that variability in the BIT indices reflects changes in the source of

374   OM. The consistently higher indices in the marls (Fig. 4c) can either be produced by greater

375   terrestrial input of brGDGTs, or by a decrease of marine crenarchaeol production. If the

376   accumulation rate is constant, the concentration of the brGDGTs can be used to distinguish

377   between a terrestrial and marine driver of BIT indices (Smith et al., 2012), i.e. more brGDGTs

378   reflect increased terrestrial input. Here, however, not only is there considerable uncertainty

379   in the accumulation rates through the lithological cycle (Nijenhuis and de Lange, 2000), but

380   also, increased fluvially-derived nutrients could both supply additional terrestrial OM

381   (additional brGDGTs) and also stimulate primary productivity, yielding higher concentrations

382 of crenarchaeol (Zell et al., 2015). GDGT concentrations, therefore, cannot be used to

383 distinguish between these two explanations, because accumulation rates cannot be

384 considered constant (variable brGDGT concentrations before the slump; Fig. 4d). However,

385 increased run-off can explain the increased BIT indices in marls due to increased terrestrial

386 OM input (Fig. 4c), while there is no obvious mechanism for an increase in crenarchaeol

387 production during limestone deposition. Therefore, we argue that, the higher marl BIT indices

388 are indicative of elevated terrigenous OM inputs (e.g. Hopmans et al., 2004).

389   Other OM proxies e.g. TAR$_{n\text{-alkanoic acid}}$ (Fig. 4c and Fig. 5e) and n-alkane concentrations

390 have similar but less consistent relationships with lithology (Fig. 5a and Fig. 6). One

391 explanation for these more ambiguous records is that they are more sensitive to changes in

392 relative preservation and within-cycle sedimentation rate changes than BIT indices.

393 Furthermore, these ratios are comprised of end-members (especially the aquatic end-

394 member) with a broad range of terrestrial and marine sources (Meyers and Arnaboldi, 2008).

395 Finally, it appears that n-alkyl lipids derive from both fluvial inputs, which would be expected

396 to track other hydrological indicators, and aeolian inputs (see section 4.3) and this mixture of

397 controls further complicates the interpretation of these data. We therefore suggest that BIT

398 indices best record the changes in OM source (i.e. Strong et al., 2012), but that other

399 biomarkers (e.g. TAR$_{n\text{-alkanes}}$; HMW n-alkane abundances), also show similar relationships.

400   As a consequence of the insolation control on lithology (Krijgsman et al., 2002), the BIT

401 indices also vary with insolation and are commonly higher during times of high insolation (Fig.

402 4c) when the marls were deposited. Numerical simulations with an ocean-atmosphere-

403 vegetation general circulation model (GCM; Marzocchi et al., 2015 and see supplementary

404 material) show a large increase in run-off from North Africa during the precession minimum

405 (insolation maximum; Fig. 8b), which is consistent with elevated terrigenous OM inputs during

406   marl deposition. A substantial component of this North African fluvial input is delivered to the

407   Eastern Mediterranean via the Nile, which could therefore have exerted a strong control on

408   sedimentary processes at Pissouri (Fig. 1). Given the proximity of Cyprus to the Nile cone, the

409   systematic changes in BIT indices with lithology, record the variability of fluvial input to the

410   Eastern Mediterranean.

411   The relationship between insolation and BIT indices explains only half of its variability

412   (R^2=0.5) and the relationships are weaker within the individual marl and limestone datasets

413   (R^2=0.24, R^2=0.26 respectively). These low regression coefficients suggest that insolation does

414   not generate a systematic gradational change in BIT indices, but instead describes a bi-modal

415   shift in the BIT-insolation relationship between the extremes of the insolation curve. Samples

416   with >0.6 BIT indices derive from parts of the precession cycles associated with insolation

417   >500 W/m^2 (these are all marls) while those with <0.3 BIT indices are associated with

418   insolation of <480 Wm^2 (all but one of these are limestones).

419   *4.3   Insolation-driven changes in plant inputs inferred from n-alkane isotopes*

420   The correlation between BIT indices and astronomically-controlled lithology suggests

421   that both the quantity and the nature of the terrestrial organic matter being supplied from

422   North Africa could change as the ITCZ shifts position, reflecting changes in the aridity/humidity

423   of the North African catchment. One mechanism for monitoring this is through *n*-alkane δ^{13}C

424   values, which increase in response to the proportion of aridity-adapted C_4 plants in the

425   depositional system (Schwab et al., 2015). There is clear evidence of a global expansion of C_4

426   plants from 8 Ma onwards although this appears to have been delayed by ~2 Myr in the

427   Eastern Mediterranean region (Edwards et al., 2010), post-dating the Pissouri section. These

428   observations dictate caution in the interpretation of even cyclic variations in leaf wax δ^{13}C

429   values. If the expansion exclusively post-dated the deposition of the study interval, we would

430   expect little leaf wax $\delta^{13}C$ sensitivity. However, this is not the case (Fig. 6). The observed

431   variation in $\delta^{13}C$ could therefore result from two interrelated factors: i) superimposed on this

432   long-term C_3-C_4transition are localised, shorter-term variations, perhaps amplified during the

433   global ecological transition and reflecting regional changes in precipitation and the advantage

434   C_4-plants have over C_3-plants in semi-arid regions (Rommerskirchen et al., 2006); or ii) changes

435   in precipitation driving similar carbon isotopic variation, although of smaller magnitude, in C_3

436   plants (Diefendorf et al., 2015). Consequently, $\delta^{13}C$ values of n-alkanes are expected to be less

437   negative during insolation minima, i.e. limestone deposition, when the ITCZ shifts further

438   south, due either to more enriched C_3 plants and/or a higher proportion of C_4 plants (Fig. 9).

439   However, this is not what we observe in the Pissouri section (Fig. 6), where the $\delta^{13}C$ values for

440   the n-alkanes of the limestones are consistently more negative than most (~80%) of the marls

441   (Fig. 6).

442   It is possible that rather than recording C_3/C_4 vegetation change driven by humidity, the

443   n-alkane $\delta^{13}C$ values of the Pissouri samples are responding to other factors, such as

444   temperature (Yamori et al., 2014) or pCO$_2$ variations (Bolton et al., 2016; Freeman and

445   Colarusso, 2001). However, while we cannot be sure that these low resolution records capture

446   the full range of precessional temperature variation, there is little evidence for pronounced

447   temperature fluctuations with insolation (Fig. 7) that could account for the pattern of n-alkane

448    $\delta^{13}C$ observed (Fig. 6). Equally, although there is evidence of pCO$_2$ decline during the Late

449   Miocene to Early Pliocene (Bolton et al., 2016), the resolution of this record is far too low (4

450   samples covering 6-8 Myr) to provide any indication that precessional fluctuations in pCO$_2$

451   could account for the n-alkane $\delta^{13}C$ record at Pissouri.

452   To explore this further, we have compared our data with inferred insolation assuming

453   little pCO$_2$ variations, and this reveals δ^{13}C variations within and between the two lithologies.

454   Within the limestone dataset, there is a clear positive relationship between insolation and the

455   carbon isotopic composition of the long-chain n-alkanes, especially n-C$_{29}$ and n-C$_{31}$ (Fig. 10).

456   It appears that at higher insolation (between 480 and 500 W/m^2), δ^{13}C values become

457   relatively stable, such that figure 10 shows two possible linear regressions for the relationship

458   between insolation and n-alkane δ^{13}C values based on either all or a subset of the limestone

459   data. The carbon isotopic compositions of the marls do not lie on the same insolation-δ^{13}C

460   regression line as the limestones, but deviate from it towards more negative values (Fig. 10)

461   and show no systematic relationship with insolation.

462   As discussed above, the positive relationship between insolation and n-alkane δ^{13}C

463   values in the limestones is unexpected, differing with model simulations of decreased rainfall

464   and expansion of C$_4$ plants during insolation minima (Fig. 9). By extension, it is apparently

465   inconsistent with our BIT indices which indicated decreased terrestrial OM inputs (i.e.

466   decreased run-off) during insolation minima. Instead, the insolation-δ^{13}C relationship during

467   the limestone deposition interval of each precessional cycle (e.g. during precession maxima

468   and insolation minima), can be explained by enhanced aeolian transport of n-alkanes from

469   the northern margin of the Mediterranean which experienced more arid conditions during

470   insolation maxima (Fig. 9; Marzocchi et al., 2015 and see supplementary material). Such an

471   interpretation is reflected in the vegetation changes seen in the GCM simulations in the

472   Anatolian Plateau (Fig.9); therefore, it appears that the n-alkane δ^{13}C records in the limestones

473   document a persistent source from the north that experienced changing vegetation, where,

474   in contrast with North Africa, there was more precipitation during insolation minima than

475   insolation maxima.

476   This relationship, however, only holds during the extreme part of the precession cycle

477   that includes the insolation minima. We suggest that during this interval, when run-off from

478   North Africa was presumably lower (Fig. 4), Pissouri was largely unaffected by North African

479   run-off and aeolian input dominated the terrestrially-derived organic matter incorporated into

480   the sediment. During insolation maxima, by contrast, the *n*-alkanes from the tropical rain

481   forests of North Africa (Holtvoeth et al., 2003) supplied the Pissouri depositional system via

482   enhanced Nile River input (Fig.9). This drove the *n*-alkane $\delta^{13}C$ values lower (Fig. 10)

483   overprinting the signal from the Anatolian Plateau.

484   ### *4.4   Long-term trends*

485   Continuous dry environments have been postulated for the lead up to the MSC

486   (Fauquette et al., 2006), inferred from Eastern Mediterranean pollen records. These show an

487   increase in *Pinus* and *Cthaya* and a decrease in tropical and sub-tropical taxa, which Faquette

488   et al. (2006) attribute to sea-level change and associated coastline variations. The increase of

489   nonacosan-10-ol concentrations which are thought to derive from pine trees (Jetter and

490   Riederer, 1995) at the top of the section could also therefore indicate a sea-level fall (Fig. 5c).

491   The dry conditions inferred from the pollen data are consistent with the small increase

492   in *n*-alkane $\delta^{13}C$ values above the slump layer (Fig. 6), especially in the longest *n*-alkanes (C_{33}),

493   that may indicate an increase in the proportion of C_4-plants due to increasing aridity or an

494   increase in $CO_{2;}$ both are favourable for a C_4 plant expansion (Freeman and Colarusso, 2001;

495   Bolton et al., 2016; Huang et al., 2007). It is also consistent with the long-term decrease in

496   limestone BIT indices (Fig. 4c), perhaps suggesting a decrease in run-off during the dry

497   extreme of the precession cycle.

498   However, the BIT record exhibits additional complexity, with three major trends/shifts

499   in the 600 kyr preceding the MSC: first, the decrease in limestone BIT indices; second, the

500   sharp decrease in marl BIT directly underneath the slump interval; and third, the increase in

501   marl BIT above the slump interval (Fig. 4c). The long-term decrease in BIT indices probably

502   reflects a gradual decrease of terrestrial OM inputs associated with increasing aridity during

503   the 500 kyr before the onset of the MSC, but an increase in crenarchaeol input cannot be

504   excluded (Fig. 4c). The concentrations of *n*-alkanes also exhibit a long-term decline, but reach

505   their lowest values below the slump layer (Fig. 5b) before increasing in the upper part of the

506   section; $TAR_{n\text{-alkanoic-acids}}$ exhibit similar trends. Therefore, in the final ~100 kyr before the MSC,

507   there appears to be divergence in the behaviour of different terrigenous OM inputs.

508   Marine faunal and floral data from Pissouri provides some insights as to the causes of

509   these long-term changes and the environmental conditions that influenced Pissouri.

510   Kouwenhoven et al. (2006) document a collapse in nannoflora at about 20 m (e.g. 6.25 Ma,

511   where the marl BIT indices decline; Fig. 5e) and a recovery just above the slump. Those

512   authors suggest that the abrupt decline in nannoflora may have been caused by a salinity

513   increase. The decline is associated with a sharp increase in the abundance of the calcareous

514   dinocyst: *Thoracosphaera* (Fig. 5e; Kouwenhoven et al., 2006). This dinocyst has been

515   described from the K/T boundary where its abundance immediately after the boundary has

516   suggested that it survived and then exploited a stressful environment as a result of either

517   considerable warming, fluctuation in salinity and pH, or higher CO_2 (Kouwenhoven et al., 2006

518   and references thierein). Of these possible causes, the occurrence of *Thoracosphaera* at

519   Pissouri probably implies higher and more fluctuating salinity conditions from 6.25 Ma

520   onwards, in line with Mediterranean-wide indicators of rising salinity in the lead up to the

521   MSC (e.g. Sierro et al., 2001). An increase in salinity, if driven by decreased freshwater inputs,

522   would be consistent with the decline in BIT indices, $TAR_{n\text{-alkanes}}$ and nonacosan-10-ol

523   abundances from 6.5 Ma to near the top of the slump at ~6.1 Ma (Fig. 4 and Fig. 5).

524   Immediately above the slump, *Thoracosphaera* abundance drops and the nannoflora

525   diversity and abundance recovers, suggesting a less extreme environment (Kouwenhoven et

526   al., 2006). Less saline conditions are consistent with the sharp increase in marl BIT indices, an

527   increase in TAR$_{n\text{-alkanes}}$ indices and the return to pre-6.25 Ma levels of brGDGT abundance

528   above the slump. The high variability in GDGTs and the sharp drop in marl BIT indices at 6.25

529   Ma (Fig. 4c) are also consistent with fluctuating salinity conditions in the Mediterranean

530   before the onset of the MSC at 5.971 Ma. *Thoracosphera* exhibits a similar increase

531   immediately before the MSC, again indicating increasing salinity.

532   Our new data are consistent with a long-term drying in the surrounding catchment, an

533   associated change in vegetation, a decrease in run-off and an associated increase in

534   Mediterranean salinity. However, the expression of these changes varies between proxy

535   records, perhaps suggesting decoupling of simple rainfall, runoff and salinity relationships. Of

536   course, this is to be expected as the MSC is not thought to have been caused solely by climate

537   change but also tectonic changes impacting the Mediterranean Sea's connection to the

538   Atlantic Ocean (Flecker et al., 2015; Achalhi et al., 2016). It appears that a combination of

539   these processes, strongly modulated by orbital forcing, dictated the evolution of

540   Mediterranean climate in the 600 kyr interval leading up to the MSC.

541   **5   Conclusions**

542   The analysis of biomarker distributions and carbon isotopic compositions in the Pissouri

543   section reveals a strong relationship with lithology and, therefore, they are also inferred to

544   respond to precession-driven insolation variation during the 600 kyr preceding the MSC. The

545   sediments deposited during inferred insolation maxima (marls) contain a greater proportion

546   of terrestrially-derived organic matter than those deposited during insolation minima

547   (limestones). BIT indices support the hypothesis that the Eastern Mediterranean experienced

548   large changes in run-off from Northern African catchments during each precessional cycle.

549   Leaf wax δ^{13}C values indicate that North Africa is not the only source of terrestrially-derived

550   organic matter and that Pissouri also received material from the northern margin of the

551   Mediterranean, probably the Anatolian Plateau in Turkey via aeolian inputs. The δ^{13}C data

552   suggest that this area was characterised by more arid vegetation, which also varied with

553   precession such that more arid conditions prevailed during periods of higher insolation, in line

554   with climate models. This arid material was supplied to Pissouri throughout the succession,

555   but it only dominates the carbon isotope signature of leaf waxes during low insolation when

556   the influence of the Nile was reduced as a result of lower discharge. The long-term trends in

557   the data indicate that the increasing salinity of the looming Messinian Salinity Crisis was

558   already apparent in the Pissouri section in the biomarker data more than 600 kyr before the

559   first gypsum precipitated and was especially clear and influential during the last 100 kyr.

560   **6   Acknowledgments**

7   References

570

571   1.   Achalhi, M., Münch, P., Cornée, J.-J., Azdimousa, A., Melinte-Dobrinescu, M., Quillévéré, F., Drinia, H.,
572   Fauquette, S., Jiménez-Moreno, G., Merzeraud, G., Moussa, A.B., El Kharim, Y., Feddi, N., 2016. The
573   Late Miocene Mediterranean-Atlantic connections through the North Rifian Corridor: New insights
574   from the Boudinar and Arbaa Taourirt basins (northeastern Rif, Morocco). Palaeogeography,
575   Palaeoclimatology, Palaeoecology 459, 131-152. doi: http://dx.doi.org/10.1016/j.palaeo.2016.06.040
576   2.   Bolton, C.T., Hernandez-Sanchez, M.T., Fuertes, M.A., Gonzalez-Lemos, S., Abrevaya, L., Mendez-
577   Vicente, A., Flores, J.A., Probert, I., Giosan, L., Johnson, J., Stoll, H.M., 2016. Decrease in
578   coccolithophore calcification and CO_2 since the middle Miocene. Nature Communications 7, 10284.
579   doi: 10.1038/ncomms10284
580   3.   Bourbonniere, R.A., Meyers, P.A., 1996. Sedimentary geolipid records of historical changes in the
581   watersheds and productivities of Lakes Ontario and Erie. Limnol Oceanogr 41, 352-359.
582   4.   Bray, E.E., Evans, E.D., 1961. Distribution of Normal-Paraffins as a Clue to Recognition of Source Beds.
583   Geochim Cosmochim Ac 22, 2-15. doi: 10.1016/0016-7037(61)90069-2
584   5.   De Jonge, C., Hopmans, E.C., Zell, C.I., Kim, J.-H., Schouten, S., Sinninghe Damsté, J.S., 2014.
585   Occurrence and abundance of 6-methyl branched glycerol dialkyl glycerol tetraethers in soils:
586   Implications for palaeoclimate reconstruction. Geochim Cosmochim Ac 141, 97-112. doi:
587   10.1016/j.gca.2014.06.013
588   6.   Diefendorf, A.F., Leslie, A.B., Wing, S.L., 2015. Leaf wax composition and carbon isotopes vary among
589   major conifer groups. Geochim Cosmochim Ac 170, 145-156. doi: 10.1016/j.gca.2015.08.018
590   7.   Edwards, E.J., Osborne, C.P., Stromberg, C.A., Smith, S.A., Consortium, C.G., 2010. The origins of C_4
591   grasslands: integrating evolutionary and ecosystem science. Science 328, 587-591. doi:
592   10.1126/science.1177216
593   8.   Eglinton, G., Hamilton, R.J., 1967. Leaf epicuticular waxes. Science 156, 1322-1335.
594   9.   Fauquette, S., Suc, J., Bertini, A., Popescu, S., Warny, S., Taoufiq, N., Villa, M., Chikhi, H., Feddi, N.,
595   Subally, D., Clauzon, G., Ferrier, J., 2006. How much did climate force the Messinian salinity crisis?
596   Quantified climatic conditions from pollen records in the Mediterranean region. Palaeogeogr Palaeocl
597   238, 281-301. doi: 10.1016/j.palaeo.2006.03.029
598   10. Flecker, R., Krijgsman, W., Capella, W., de Castro Martíns, C., Dmitrieva, E., Mayser, J.P., Marzocchi, A.,
599   Modestou, S., Lozano, D.O., Simon, D., Tulbure, M., van den Berg, B., van der Schee, M., de Lange, G.,
600   Ellam, R., Govers, R., Gutjahr, M., Hilgen, F., Kouwenhoven, T., Lofi, J., Meijer, P., Sierro, F.J., Bachiri, N.,
601   Barhoun, N., Alami, A.C., Chacon, B., Flores, J.A., Gregory, J., Howard, J., Lunt, D., Ochoa, M., Pancost,
602   R., Vincent, S., Yousfi, M.Z., 2015. Evolution of the Late Miocene Mediterranean-Atlantic gateways and
603   their impact on regional and global environmental change. Earth-Sci Rev. doi:
604   10.1016/j.earscirev.2015.08.007
605   11. Freeman, K.H., Colarusso, L.A., 2001. Molecular and isotopic records of C_4 grassland expansion in the
606   Late Miocene. Geochim Cosmochim Ac 65, 1439-1454. doi: 10.1016/s0016-7037(00)00573-1
607   12. Hilgen, F.J., Krijgsman, W., Langereis, C.G., Lourens, L.J., 1997. Breakthrough made in dating of the
608   geological record. Eos, Transactions American Geophysical Union 78, 285. doi: 10.1029/97eo00186
609   13. Holtvoeth, J., Wagner, T., Schubert, C.J., 2003. Organic matter in river-influenced continental margin
610   sediments: The land-ocean and climate linkage at the Late Quaternary Congo fan (ODP Site 1075).
611   Geochemistry, Geophysics, Geosystems 4. doi: 10.1029/2003gc000590
612   14. Hopmans, E.C., Schouten, S., Pancost, R.D., van der Meer, M.T., Sinninghe Damste, J.S., 2000. Analysis
613   of intact tetraether lipids in archaeal cell material and sediments by high performance liquid
614   chromatography/atmospheric pressure chemical ionization mass spectrometry. Rapid Commun Mass
615   Spectrom 14, 585-589. doi: 10.1002/(SICI)1097-0231(20000415)14:7<585::AID-RCM913>3.0.CO;2-N
616   15. Hopmans, E.C., Weijers, J.W.H., Schefuss, E., Herfort, L., Damste, J.S.S., Schouten, S., 2004. A novel
617   proxy for terrestrial organic matter in sediments based on branched and isoprenoid tetraether lipids.
618   Earth Planet Sc Lett 224, 107-116. doi: 10.1016/j.epsl.2004.05.012
619   16. Huang, Y., Clemens, S.C., Liu, W., Wang, Y., Prell, W.L., 2007. Large-scale hydrological change drove the
620   late Miocene C_4 plant expansion in the Himalayan foreland and Arabian Peninsula. Geology 35, 531.
621   doi: 10.1130/G23666A.1
622   17. Huguet, C., Kim, J.-H., de Lange, G.J., Sinninghe Damsté, J.S., Schouten, S., 2009. Effects of long term
623   oxic degradation on the, TEX_{86} and BIT organic proxies. Organic Geochemistry 40, 1188-1194. doi:
624   10.1016/j.orggeochem.2009.09.003

18. Huguet, C., Hopmans, E.C., Febo-Ayala, W., Thompson, D.H., Sinninghe Damsté, J.S., Schouten, S., 2006. An improved method to determine the absolute abundance of glycerol dibiphytanyl glycerol tetraether lipids. Org Geochem 37, 1036-1041. doi: 10.1016/j.orggeochem.2006.05.008

19. Jetter, R., Riederer, M., 1995. In vitro Reconstitution of Epicuticular Wax Crystals: Formation of Tubular Aggregates by Long-Chain Secondary Alkanediols. Botanica Acta 108, 111-120. doi: 10.1111/j.1438-8677.1995.tb00840.x

20. Kidd, R.B., Cita, M.B., Ryan, W.B.F., 1978. Stratigraphy of Eastern Mediterranean sapropel sequences recovered during DSDP 42A and their palaeoenvioromental significance.

21. Kim, J.H., van der Meer, J., Schouten, S., Helmke, P., Willmott, V., Sangiorgi, F., Koc, N., Hopmans, E.C., Damste, J.S.S., 2010. New indices and calibrations derived from the distribution of crenarchaeal isoprenoid tetraether lipids: Implications for past sea surface temperature reconstructions. Geochimica Et Cosmochimica Acta 74, 4639-4654. doi: 10.1016/j.gca.2010.05.027

22. Kouwenhoven, T.J., Morigi, C., Negri, A., Giunta, S., Krijgsman, W., Rouchy, J.M., 2006. Paleoenvironmental evolution of the eastern Mediterranean during the Messinian: Constraints from integrated microfossil data of the Pissouri Basin (Cyprus). Mar Micropaleontol 60, 17–44. doi: 10.1016/j.marmicro.2006.02.005

23. Kouwenhoven, T.J, Hilgen, F. J., van der Zwaan, G. J.,2003. Late Tortonian-early Messinian stepwise disruption of the Mediterranean-Atlantic connections: constraints from benthic foraminiferal and geochemical data. Palaeogeography Palaeoclimatology Palaeoecology 198, 303-319. doi: 10.1016/S0031-0182(03)00482-3

24. Krijgsman, W., Blanc-Valleron, M.M., Flecker, R., Hilgen, F.J., Kouwenhoven, T.J., Merle, D., Orszag-Sperber, F., Rouchy, J.M., 2002. The onset of the Messinian salinity crisis in the Eastern Mediterranean (Pissouri Basin, Cyprus). Earth Planet Sc Lett 194, 299-310. doi: 10.1016/S0012-821x(01)00574-X

25. Kutzbach, J.E., Chen, G., Cheng, H., Edwards, R.L., Liu, Z., 2014. Potential role of winter rainfall in explaining increased moisture in the Mediterranean and Middle East during periods of maximum orbitally-forced insolation seasonality. Climate Dynamics 42, 1079-1095. doi: 10.1007/s00382-013-1692-1

26. Larrasoaña J.C., Roberts, A. P., Rohling, E. J., 2013. Dynamics of Green Sahara Periods and Their Role in Hominin Evolution. PLoSONE 8, doi: 10.1371/journal.pone.0076514

27. Laskar, J., Robutel, P., Joutel, F., Gastineau, M., Correia, A.C.M., Levrard, B., 2004. A long-term numerical solution for the insolation quantities of the Earth. Astronomy and Astrophysics 428, 261-285. doi: 10.1051/0004-6361:20041335

28. Manzi, V., Gennari, R., Hilgen, F., Krijgsman, W., Lugli, S., Roveri, M., Sierro, F.J., 2013. Age refinement of the Messinian salinity crisis onset in the Mediterranean. Terra Nova 25, 315-322. doi: 10.1111/Ter.12038

29. Marzocchi, A., Lunt, D.J., Flecker, R., Bradshaw, C.D., Farnsworth, A., Hilgen, F.J., 2015. Orbital control on Late Miocene climate and the North African monsoon: insight from an ensemble of sub-precessional simulations. Climate of the Past Discussions 11, 2181-2237. doi: 10.5194/cpd-11-2181-2015

30. Meyers, P.A., Arnaboldi, M., 2008. Paleoceanographic implications of nitrogen and organic carbon isotopic excursions in mid-Pleistocene sapropels from the Tyrrhenian and Levantine Basins, Mediterranean Sea. Palaeogeogr Palaeocl 266, 112-118. doi: 10.1016/j.palaeo.2008.03.018

31. Nijenhuis, I.A., de Lange, G.J., 2000. Geochemical constraints on Pliocene sapropel formation in the eastern Mediterranean. Mar Geol 163, 41-63. doi: 10.1016/s0025-3227(99)00093-6

32. O'Leary, M.H., 1981. Carbon isotope fractionation in plants. Phytochemistry 20, 553-567. doi: 10.1016/0031-9422(81)85134-5

33. Peterse, F., van der Meer, J., Schouten, S., Weijers, J.W.H., Fierer, N., Jackson, R.B., Kim, J.-H., Sinninghe Damsté, J.S., 2012. Revised calibration of the MBT–CBT paleotemperature proxy based on branched tetraether membrane lipids in surface soils. Geochim Cosmochim Ac 96, 215-229. doi: 10.1016/j.gca.2012.08.011

34. Rohling, E.J., Marino, G., Grant, K.M., 2015. Mediterranean climate and oceanography, and the periodic development of anoxic events (sapropels). Earth-Sci Rev 143, 62-97. doi: 10.1016/j.earscirev.2015.01.008

35. Rommerskirchen, F., Eglinton, G., Dupont, L., Rullkotter, J., 2006. Glacial/interglacial changes in southern Africa: Compound-specific $\delta^{13}C$ land plant biomarker and pollen records from southeast Atlantic continental margin sediments. Geochemistry Geophysics Geosystems 7. doi: Artn Q0801010.1029/2005gc001223

682   36. Rossignol-Strick, M., 1985. Mediterranean Quaternary Sapropels, an Immediate Response of the
683   African Monsoon to Variation of Insolation. Palaeogeogr Palaeocl 49, 237-263. doi: 10.1016/0031-
684   0182(85)90056-2
685   37. Schouten, S., Hopmans, E.C., Sinninghe Damsté, J.S., 2013. The organic geochemistry of glycerol dialkyl
686   glycerol tetraether lipids: A review. Org Geochem 54, 19-61. doi: 10.1016/j.orggeochem.2012.09.006
687   38. Schwab, V.F., Garcin, Y., Sachse, D., Todou, G., Séné, O., Onana, J.-M., Achoundong, G., Gleixner, G.,
688   2015. Effect of aridity on δ^{13}C and δD values of C_3 plant- and C_4 graminoid-derived leaf wax lipids from
689   soils along an environmental gradient in Cameroon (Western Central Africa). Org Geochem 78, 99-109.
690   doi: 10.1016/j.orggeochem.2014.09.007
691   39. Sierro, F.J., Hilgen, F.J., Krijgsman, W., Flores, J.A., 2001. The Abad composite (SE Spain): a Messinian
692   reference section for the Mediterranean and the APTS. Palaeogeogr Palaeocl 168, 141-169. doi:
693   10.1016/S0031-0182(00)00253-4
694   40. Sinninghe Damsté, J.S., Schouten, S., Hopmans, E.C., van Duin, A.C., Geenevasen, J.A., 2002.
695   Crenarchaeol: the characteristic core glycerol dibiphytanyl glycerol tetraether membrane lipid of
696   cosmopolitan pelagic crenarchaeota. J Lipid Res 43, 1641-1651. doi: 10.1194/jlr.M200148-JLR200
697   41. Smith, R.W., Bianchi, T.S., Li, X., 2012. A re-evaluation of the use of branched GDGTs as terrestrial
698   biomarkers: Implications for the BIT Index. Geochim Cosmochim Ac 80, 14-29. doi
699   10.1016/j.gca.2011.11.025
700   42. Strong, D.J., Flecker, R., Valdes, P.J., Wilkinson, I.P., Rees, J.G., Zong, Y.Q., Lloyd, J.M., Garrett, E.,
701   Pancost, R.D., 2012. Organic matter distribution in the modern sediments of the Pearl River Estuary.
702   Org Geochem 49, 68-82. doi: 10.1016/j.orggeochem.2012.04.011
703   43. Sugden, W., McKerrow, W.S., 1962. The Composition of Marls and Limestones in the Great Oolite
704   Series of Oxfordshire. Geological Magazine 99, 363. doi: 10.1017/s0016756800058477
705   44. Tierney, J.E., Tingley, M.P., 2015. A TEX_{86} surface sediment database and extended Bayesian
706   calibration. Scientific data 2, 150029. doi: 10.1038/sdata.2015.29
707   45. Toucanne, S., Angue Minto'o, C.M., Fontanier, C., Bassetti, M.-A., Jorry, S.J., Jouet, G., 2015. Tracking
708   rainfall in the northern Mediterranean borderlands during sapropel deposition. Quaternary Sci Rev
709   129, 178-195. doi: 10.1016/j.quascirev.2015.10.016
710   46. Tzanova, A., Herbert, T.D., Peterson, L., 2015. Cooling Mediterranean sea surface temperatures during
711   the Late Miocene provide a climate context for evolutionary transitions in Africa and Eurasia. Earth
712   Planet Sc Lett 419, 71-80. doi: 10.1016/j.epsl.2015.03.016
713   47. Weijers, J.W.H., Schouten, S., van den Donker, J.C., Hopmans, E.C., Damste, J.S.S., 2007. Environmental
714   controls on bacterial tetraether membrane lipid distribution in soils. Geochim Cosmochim Ac 71, 703-
715   713. doi: 10.1016/j.gca.2006.10.003
716   48. Yamori, W., Hikosaka, K., Way, D.A., 2014. Temperature response of photosynthesis in C_3, C_4, and CAM
717   plants: temperature acclimation and temperature adaptation. Photosynth Res 119, 101-117. doi:
718   10.1007/s11120-013-9874-6
719   49. Yang, H., Pancost, R.D., Dang, X.Y., Zhou, X.Y., Evershed, R.P., Xiao, G.Q., Tang, C.Y., Gao, L., Guo, Z.T., Xie,
720   S.C., 2014. Correlations between microbial tetraether lipids and environmental variables in Chinese
721   soils: Optimizing the paleo-reconstructions in semi-arid and arid regions. Geochim Cosmochim Ac 126,
722   49-69. doi: 10.1016/j.gca.2013.10.041
723   50. Zell, C., Kim, J.-H., Dorhout, D., Baas, M., Sinninghe Damsté, J.S., 2015. Sources and distributions of
724   branched tetraether lipids and crenarchaeol along the Portuguese continental margin: Implications for
725   the BIT index. Continental Shelf Research. doi: 10.1016/j.csr.2015.01.006
726

727   **8   Figures**

728

729   Figure 1: Map showing the inflow of the Nile into the Mediterranean and the location

730   of the Pissouri Section on Cyprus (34°40'01.9"N; 32°38'48.8"E). A photograph of the section

731   before it was sprayed with concrete is given on the right.
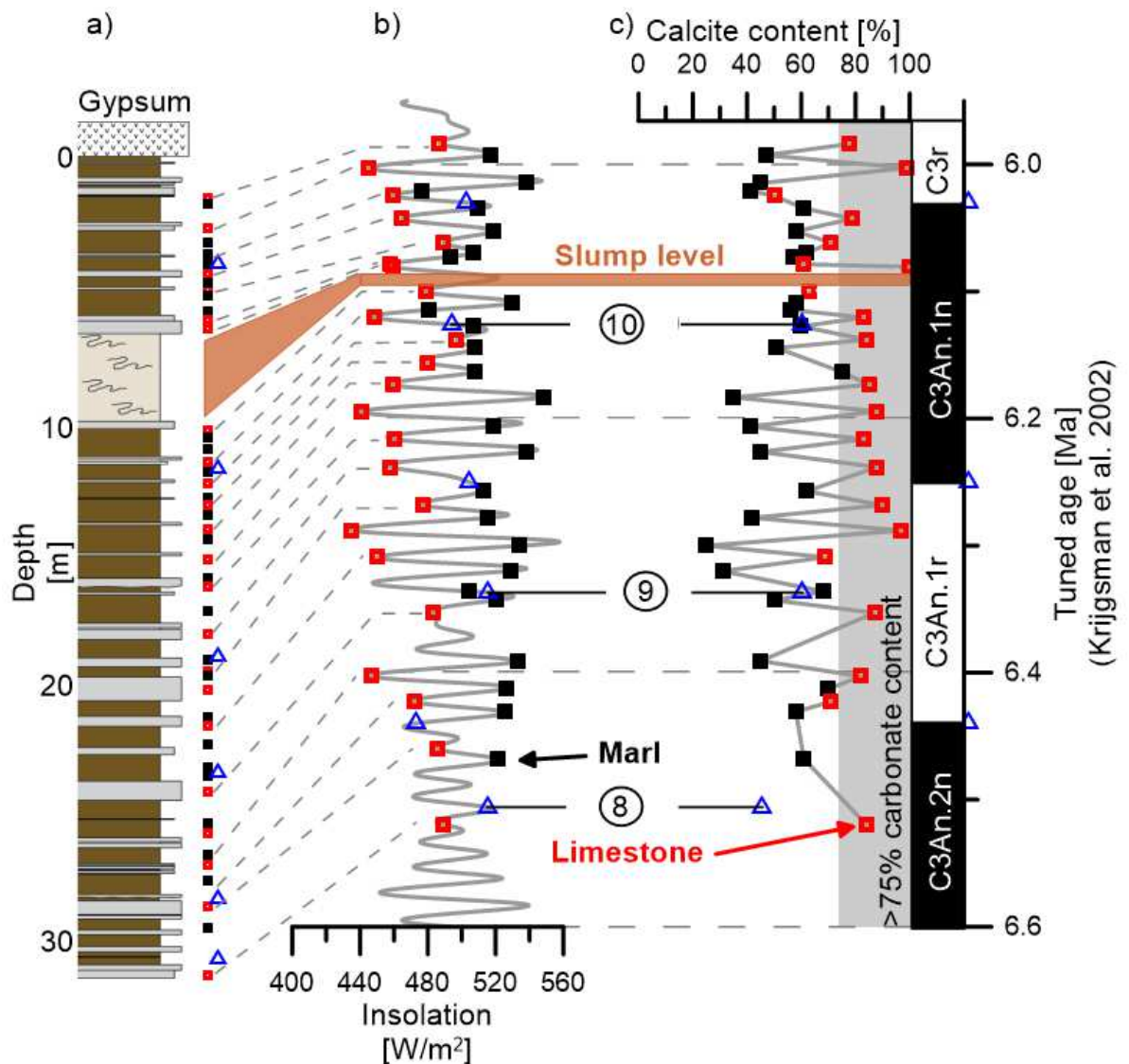
732

Figure 2: Schematic log of the Pissouri section (a) with alternating harder (grey and softer (brown)layers alongside (b) the insolation curve (Laskar et al., 2004) and (c) the calcium carbonate content of the sediment which was used for astronomical tuning of the section (Krijgsman et al., 2002). The biostratigraphic tie points (blue triangles) shown from Krijgsman et al. (2002) are: (8) the LO of the *G. miotumida* group (6.506 Ma); (9) the sinistral/dextral coiling change of *Neogloboquadrina acostaensis* (6.337 Ma); and (10) the first infux (>80%) of sinistral neogloboquadrinids (6.126 Ma). The palaeomagnetic tie points (blue triangles) are C3r-C3An.1n (6.03 Ma) C3An.1n-C3An.1r (6.25 Ma) C3An.1r-C3An.2n (6.44 Ma; Krijgsman et al., 2002). The vertical grey bar reflects >75% carbonate content, the formal definition of a

743   limestone (Sugden and McKerrow, 1962). A slump layer (brown bar) interrupts the cyclic

744   limestone-marl alternations between 7 and 10 m depth (Krijgsman et al., 2002).

745
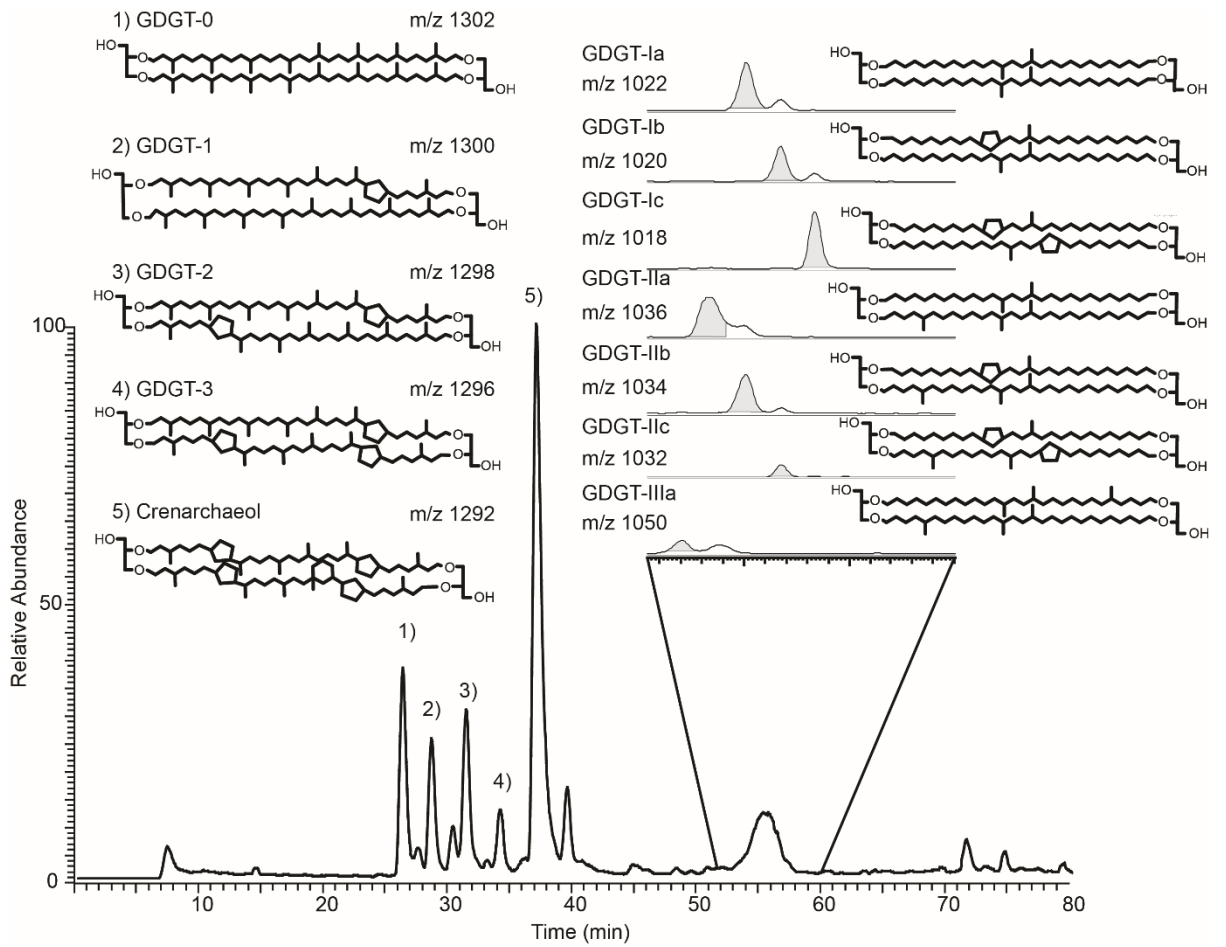
Figure 3: Representative HPLC-APCI-MS chromatogram of a Pissouri limestone (RF-7018; data table) showing both br- and iGDGTs with their respective *m/z*. Note that the brGDGT peak in this particular total ion content trace is dominated by GDGT-Ia
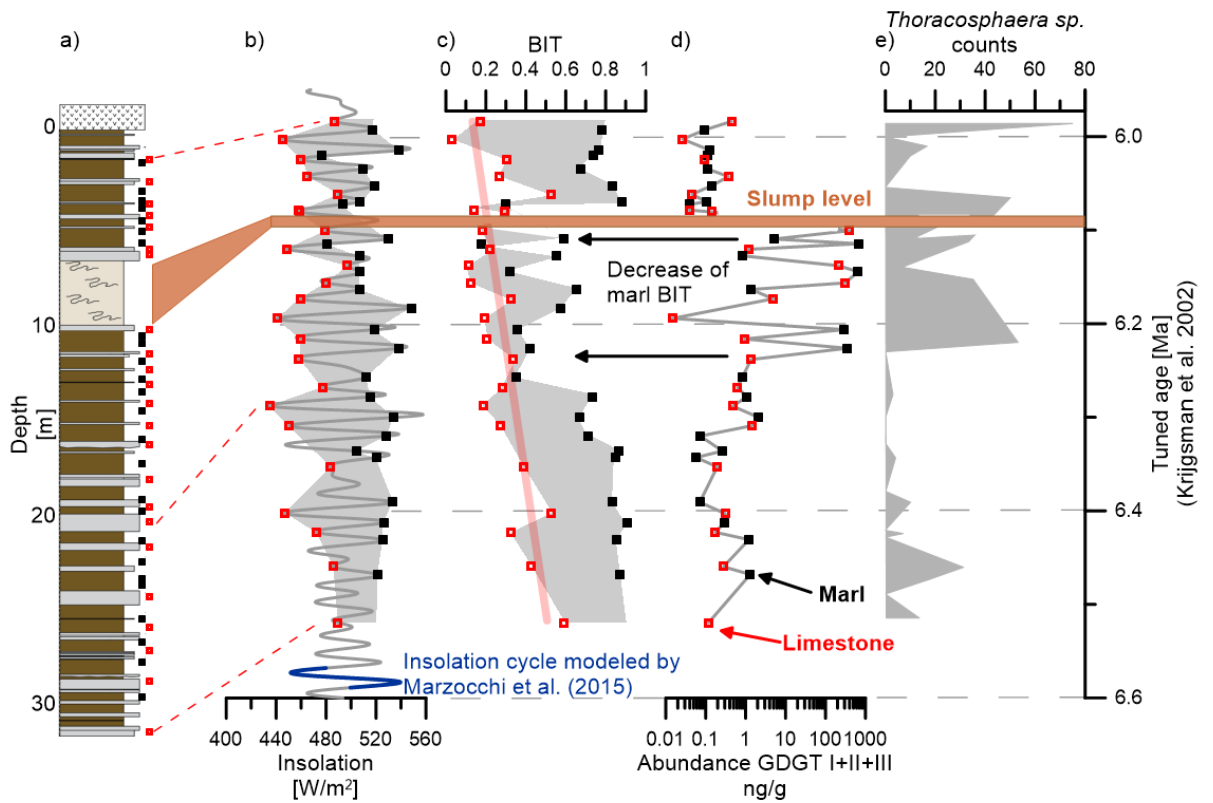
Figure 4: A schematic log (a) of the Pissouri section (Krijgsman et al., 2002) showing sampled levels: limestones (red squares) and marls (black squares). Aligned with the log are (b) the 65N insolation curve (Laskar et al., 2004) with the specific cycle used for the General Circulation Model simulations indicated in blue (Marzocchi et al., 2015), (c) BIT indices, including the long-term trend through the limestone data, (d) brGDGT abundances and (e) counts for the calcareous dinocyst *Thoracosphaera sp.* (Kouwenhoven et al., 2006).

759
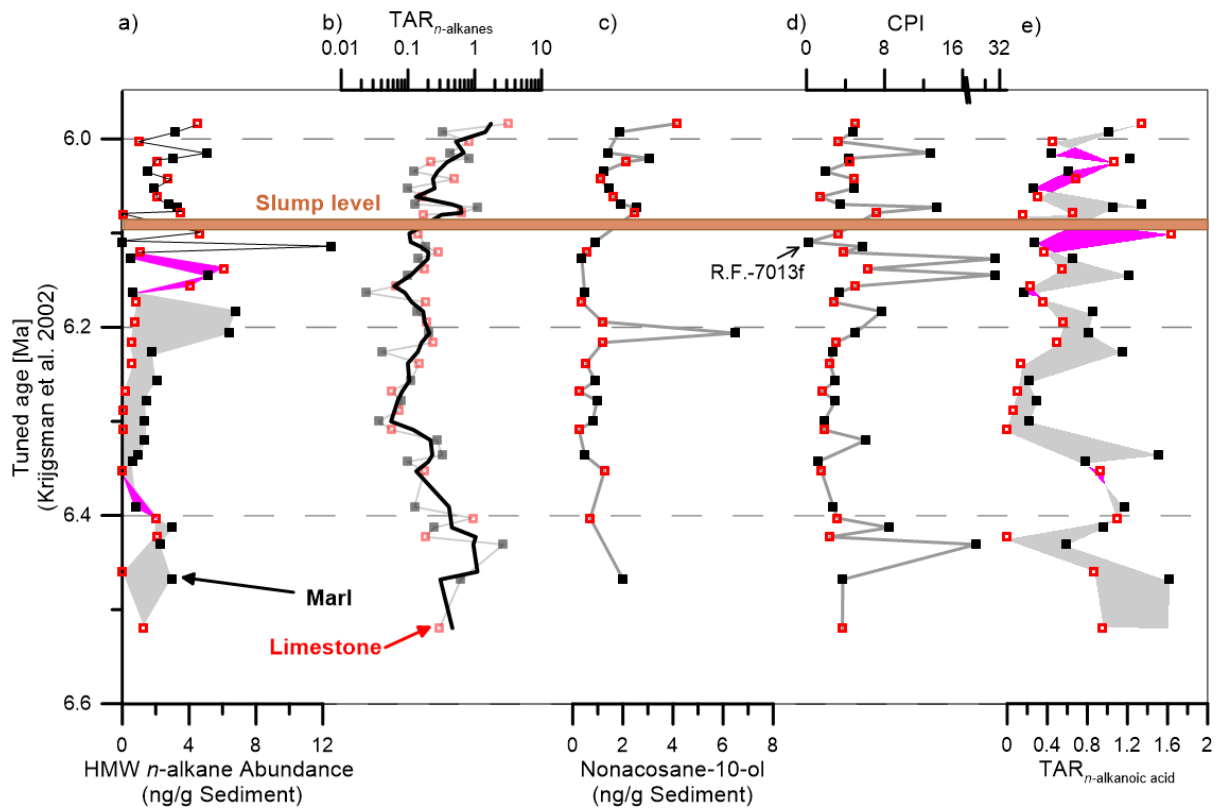
Figure 5: Alkyl biomarker records through the Pissouri section including (a) HMW n-alkane (C_{29}+C_{31}+C_{33}) concentrations; (b) the TAR$_{n\text{-alkanes}}$ with a three point running average; the (c) nonacosan-10-ol concentrations; (d) the CPI of the n-alkanes with the excluded sample R.F.713f highlighted; and (e) the TAR$_{n\text{-alkanoic acid}}$. Grey sh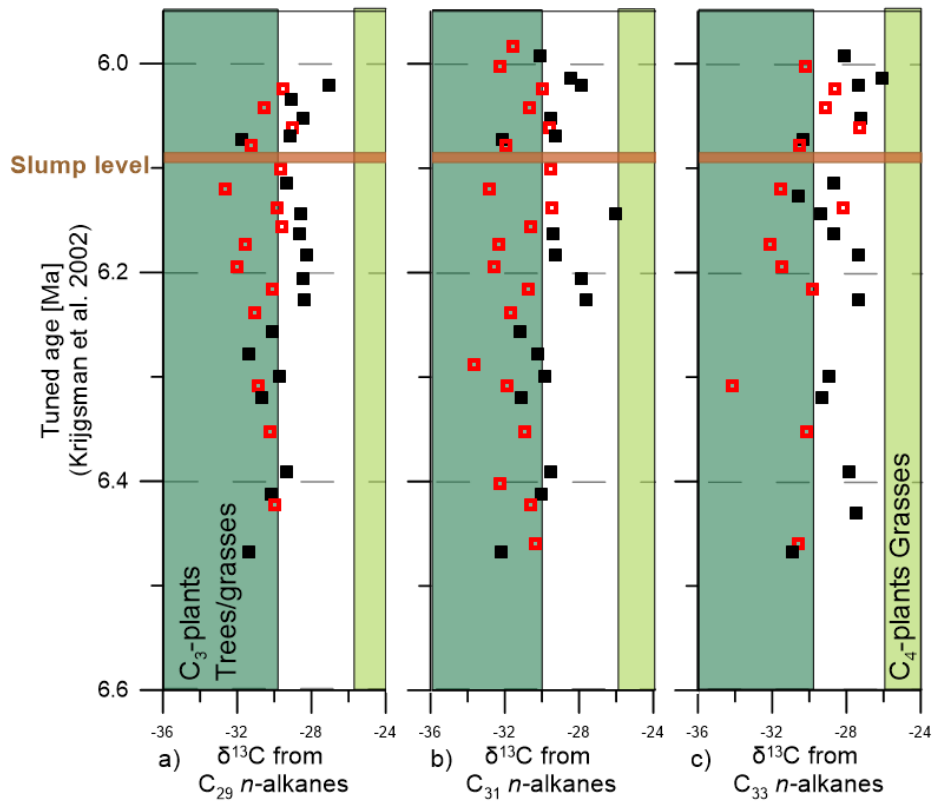ading indicates higher marl values relative to limestones, whereas magenta indicates higher values for limestones than adjacent marls.

767

Figure 6: Age profiles of the (a) C_{29}, (b) C_{31}, and (c) C_{33} n-alkane $\delta^{13}C$ values as well as that of (d) the combined abundances of those three n-alkanes. The stable carbon isotopic composition of leaf waxes are dependent on the biosynthetic pathway of the source plant (O'Leary, 1981). A typical distribution for $\delta^{13}C$ values of C_{29}-C_{31} n-alkanes from leaf waxes of C_3 and C_4 plants is given as green shading (modified after Rommerskirchen et al., 2006).
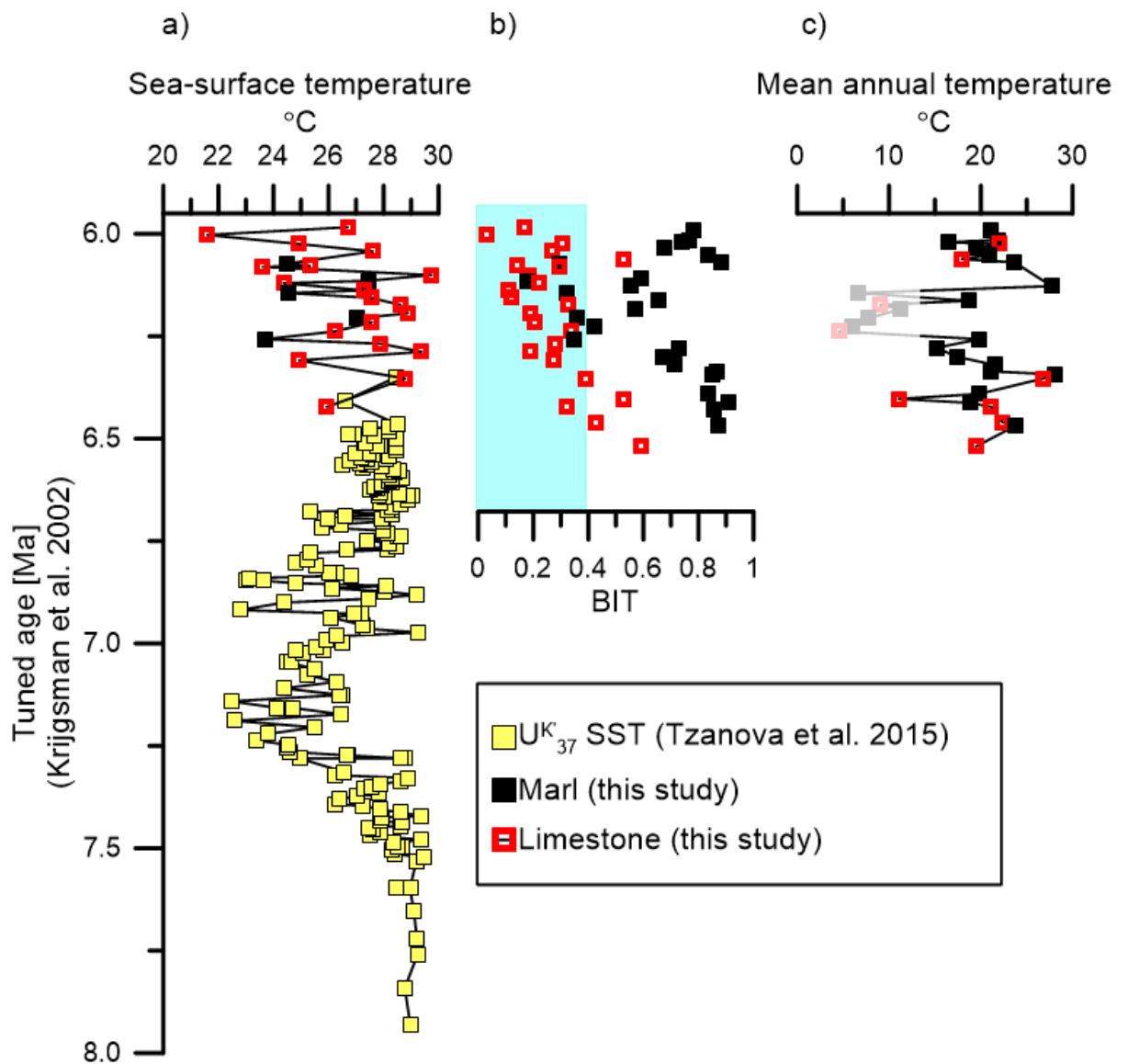
773

774   Figure 7: The SST profile (a) derived from GDGTs (TEX$_{86}$, this study) at Pissouri and

775   alkenones (U$^{K'}$37, Tzanova et al., 2015) from Monte dei Corvi, Italy. TEX$_{86}$ data are limited to

776   those samples with BIT < 0.4 from Pissouri. Also shown are limestone and marl BIT indices (b;

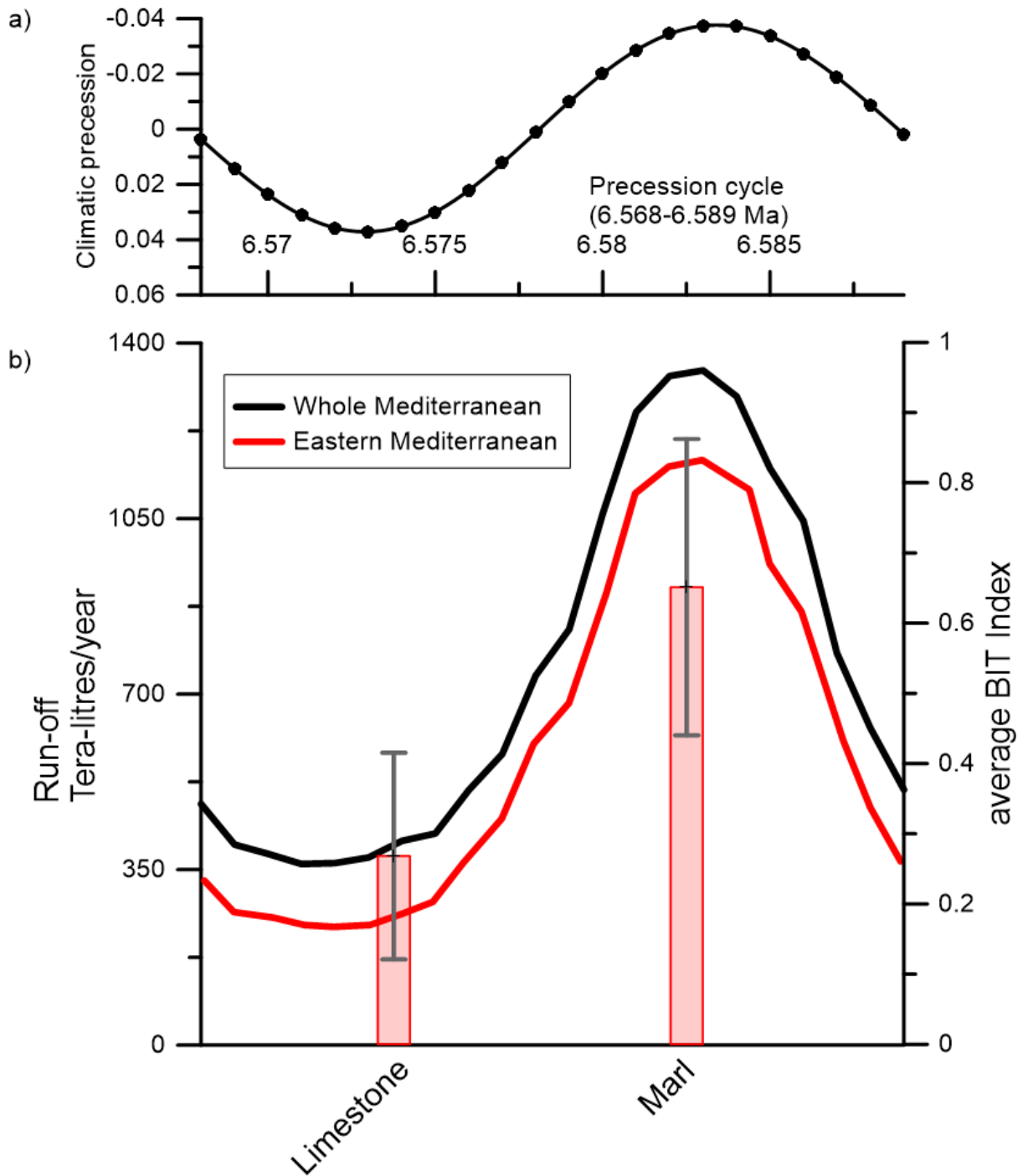777   with BIT <0.4 shaded in turquoise) and (c) limestone and marl MBT'/CBT-derived MAT (Peterse

778   et al., 2012) for samples with BIT>0.3. The shaded area in grey marks the decrease in marl BIT

779   area.

780

781

782   Figure 8: Climate Model-derived run-off into the Mediterranean as a whole (black line)

783   and Eastern Mediterranean (red line) and its relationship with precession-forced insolation

784   over one precession cycle (Marzocchi et al., 2015 and see supplementary material). The bar

785   chart shows the average and standard deviation of the BIT indices in the limestones and the

786   marls throughout the entire section.

787
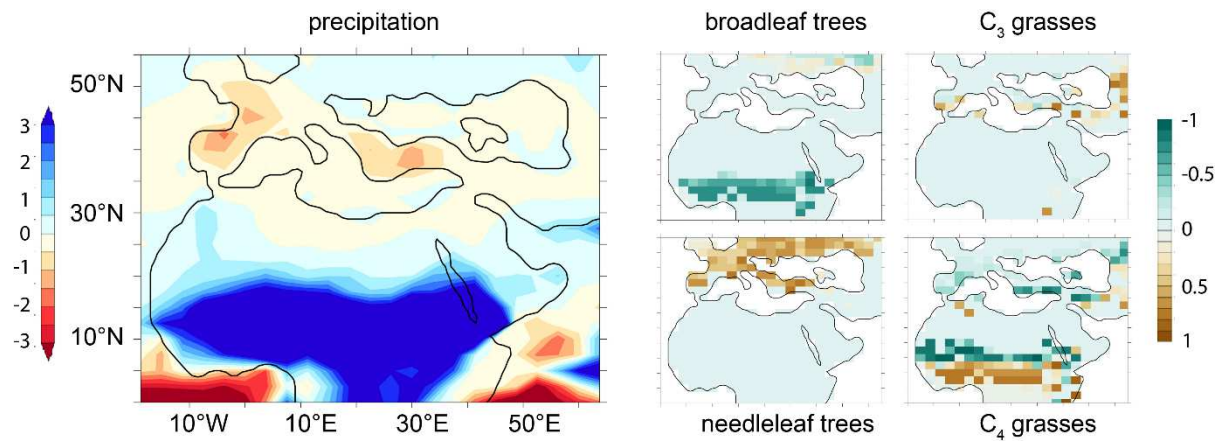
Figure 9: Precipitation differences between precession minima (insolation maxima) and precession maxima (insolation minima) across N. Africa and the Mediterranean, simulated using HadCM3L with coupled ocean, atmosphere and vegetation (Marzocchi et al., 2015). The four smaller panels show vegetation changes between precession minima and precession maxima for broadleaf trees, needle leaf trees, C3-plants and C4-plants (Marzocchi et al., 2015 and see supplementary material).
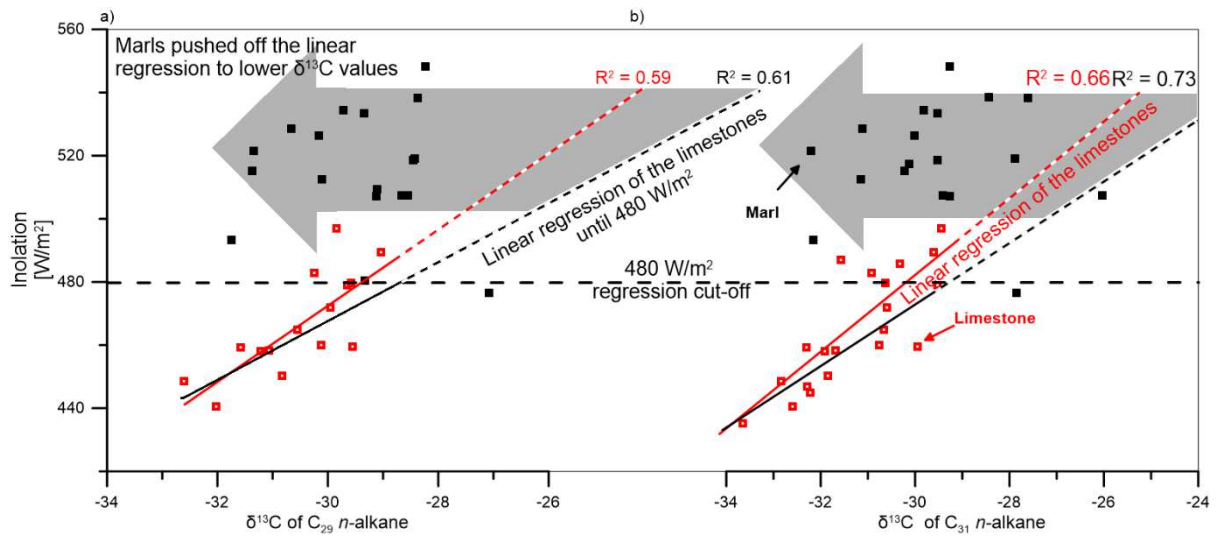
795

796   Figure 10: Cross-plot of insolation versus leaf wax $\delta^{13}C$ values, showing the different

797   relationships for the marls (black) and the limestones (red) for a) C_{29} and b) C_{31} n-alkanes. The

798   linear regressions of the limestones are indicated (red for all limestones and black for

799   limestones beneath 480 W/m^2, above which the relationship appears to break down). Both

800   regressions are extrapolated to higher insolation by dashed lines. The offset of the leaf wax

801   $\delta^{13}C$ values to lower values in the marls is indicated with the grey arrow. The absolute

802   insolation is derived from astronomical tuning of the Pissouri Section (Krijgsman et al., 2002).